THE JOURNAL OF PHYSICAL CHEMISTRY C

Article

pubs.acs.org/JPCC

Fluorescent Carbon Nanotube Defects Manifest Substantial Vibrational Reorganization

Mijin Kim,[†] Lyudmyla Adamska,[‡,§] Nicolai F. Hartmann,[‡] Hyejin Kwon,[†] Jin Liu,[‡,§] Kirill A. Velizhanin,[§] Yanmei Piao,[†] Lyndsey R. Powell,[†] Brendan Meany,[†] Stephen K. Doorn,[*,‡] Sergei Tretiak,[‡,§] and YuHuang Wang[*,†]

[†]Department of Chemistry and Biochemistry, University of Maryland, College Park, Maryland 20742, United States

[‡]Center for Integrated Nanotechnologies, Materials Physics and Applications Division, and [§]T-1, Physics and Chemistry of Materials, Theoretical Division, Los Alamos National Laboratory, Los Alamos, New Mexico 87545, United States

Supporting Information

ABSTRACT: Fluorescent defects have opened up exciting new opportunities to chemically tailor semiconducting carbon nanotubes for imaging, sensing, and photonics needs such as lasing, single photon emission, and photon upconversion. However, experimental measurements on the trap depths of these defects show a puzzling energy mismatch between the optical gap (difference in emission energies between the native exciton and defect trap states) and the thermal detrapping energy determined by application of the van 't Hoff equation. To resolve this fundamentally important problem, here we synthetically incorporated a series of fluorescent aryl defects into semiconducting single-walled carbon nanotubes and experimentally determined their energy levels by temperature-dependent and chemically correlated evolution of exciton population and photoluminescence. We found that depending on the chemical nature and density of defects, the exciton detrapping energy is 14−77% smaller than the optical gap determined from photoluminescence. For the same type of defect, the detrapping energy increases with defect density from 76 to 131 meV for 4-nitroaryl defects in (6,5) single-walled carbon nanotubes, whereas the optical gap remains nearly unchanged (<5 meV). These experimental findings are corroborated by quantum-chemical simulations of the chemically functionalized carbon nanotubes. Our results suggest that the energy mismatch arises from vibrational reorganization due to significant deformation of the nanotube geometry upon exciton trapping at the defect site. An unexpectedly large reorganization energy (on the order of 100 meV) is found between ground and excited states of the defect tailored nanostructures. This finding reveals a molecular picture for description of these synthetic defects and suggests significant potential for tailoring the electronic properties of carbon nanostructures through chemical engineering.

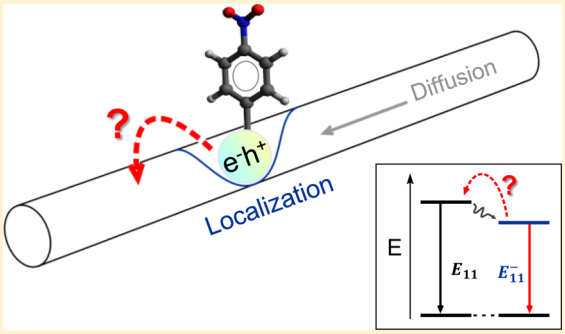

INTRODUCTION

Fluorescent aryl defects are emerging synthetic structures that open opportunities to experimentally probe defects and fundamentally understand the effects of chemical functionalization on low-dimensional materials.[1] The defects can be chemically created in semiconducting single-walled carbon nanotubes (SWCNTs) through covalent attachment of a small number of aryl functional groups that produce sparsely decorated sp^3 defects in the sp^2 lattice of the nanostructure. Fluorescent defects can also be introduced *via* oxygen doping[2] and sidewall alkylation,[3] although defects produced by these two methods are less bright and generally lack the chemical tunability available through substituted aryl defects. Experimental results from our lab have shown that a carefully incorporated aryl defect splits the doubly degenerate frontier orbitals, producing a new, low-lying, fluorescent state (E_{11}^{-}).[1] Such fluorescent defects can trap a mobile exciton (Figure 1),[4−6] allowing the localized exciton to radiatively relax *via* E_{11}^{-} photoluminescence (PL). The defect PL occurs at red-shifted energies from the native lowest-energy excitonic transition (E_{11}).[1−3] The energy difference between E_{11}^{-} and E_{11} is denoted here as $\Delta E_{optical}$.

The unique optical properties of these fluorescent defects have spurred intensive investigations on exciton trapping and brightening at defect sites.[4−10] Beyond a desire to understand the origins and behavior of this novel emission, studies are motivated by new promise the defect emission holds for photonic, optoelectronic, sensing, and imaging applications, afforded by potential for enhanced quantum yields[1−5] and new functionality[11,12] and as photon upconversion[13] and quantum light sources.[14,15] An important aspect of the defect-induced photophysics that remains to be understood is determining the

Received: March 10, 2016
Revised: May 3, 2016
Published: May 3, 2016

DOI: 10.1021/acs.jpcc.6b02538
J. Phys. Chem. C 2016, 120, 11268−11276

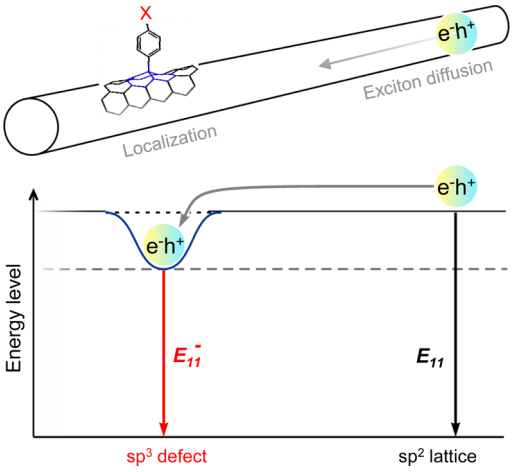

Figure 1. Schematic of defect-modulated exciton diffusion and recombination.

factors underlying the exciton trapping; in particular, what is the depth of the trapping potential, and how does it impact observed behavior? Trap depth is a determining factor in such fundamental behavior as degree of exciton localization and for relaxation processes or impact on band positions (of relevance to dopant-site redox behavior and potential impact on energy harvesting ability).[9] Trap depth can also impact the quality and stability of defect photoluminescence (PL) emission.[6,14] Furthermore, thermal detrapping is an important step in recently observed photon upconversion from similarly defect-engineered SWCNTs.[13] Studies of thermally induced exciton detrapping in oxygen-doped and alkylated nanotubes indicate the trap depth is significantly lower, with detrapping energies ($\Delta E_{thermal}$) being less than 50% of $\Delta E_{optical}$.[2,10] Combined experimental and theoretical studies of the defect-site redox behaviors also indicate a reduction in bandgap that is significantly smaller than the associated optical energy shift.[9] While a simplistic picture of ground-state perturbation of exciton energies at the oxygen dopant site provides an initial understanding of the difference in observed energies,[2] the origin of the large discrepancy between $\Delta E_{optical}$ and $\Delta E_{thermal}$ is not yet established.

Herein, we quantitatively probe the thermal activation of defect-trapped excitons as a function of the chemical nature and density of defects and generalize the behavior to a new class of defects. A series of fluorescent aryl defects were chemically created in (6,5)-SWCNTs through controlled diazonium chemistry.[1] Detrapping energies ($\Delta E_{thermal}$) for each defect type are derived from van 't Hoff plots constructed based on the intensity ratio of the lowest energy SWCNT exciton emission (E_{11}) and defect PL (E_{11}^-) as a function of temperature. The measured detrapping energies are directly correlated with the optical gaps ($\Delta E_{optical}$) determined from defect photoluminescence. We found that both $\Delta E_{optical}$ and $\Delta E_{thermal}$ are linearly dependent on the electron-withdrawing nature of specific functional groups, as measured by the Hammett substituent constant (σ_p). At relatively high defect densities, $\Delta E_{thermal}$ is more than half of $\Delta E_{optical}$. However, we found a strong dependence of the energy mismatch on defect density, with differences between $\Delta E_{thermal}$ and $\Delta E_{optical}$ on the order of 100 meV found in the low-density limit. On the basis of these observations, we propose a theory that highlights as the origin of the $\Delta E_{thermal}/\Delta E_{optical}$ energy difference a substantial vibrational reorganization energy between the excited and ground state of SWCNTs in the presence of a fluorescent defect. This proposed origin is supported by density functional theory (DFT) calculations of reorganization energies that agree with the experimental trends and magnitude of measured trapping energies.

EXPERIMENTAL SECTION

Chirality-Enriched Carbon Nanotubes. HiPco SWCNTs (Rice University, batch #194.3) were sorted using Sephacryl S-200 high resolution chromatography resin (GE Healthcare), as described previously,[16] to produce (6,5)-SWCNT enriched samples. The purified SWCNTs were stabilized as individual nanotubes in deuterium oxide (D_2O) (Cambridge Isotope Laboratories, Inc., 99.8%) by 1 wt % sodium dodecyl sulfate (SDS) for subsequent studies. Alternatively, an aqueous two-phase (ATP) separation process[17,18] was used to also generate (6,5)-SWCNT enriched material used for doping with ozone and covalent functionalization with 3,5-dichlorobenzene-diazonium tetrafluoroborate ($3,5\text{-}C_6H_3Cl_2N_2^+\cdot BF_4^-$). After chirality isolation the SWCNTs were exchanged into 1 wt % SDS in Millipore H_2O or 1 wt % sodium dodecylbenzene-sulfonate (SDBS) in Millipore H_2O surfactant environment *via* pressure filtration (100 kDa regenerated cellulose membrane).

Chemical Creation of Fluorescent Aryl Defects in SWCNTs. Aryl defects were created through controlled functionalization of SWCNTs with aryl diazonium salts as we previously described.[1] We note that a modified functionalization protocol[6] was used for (6,5)-SWCNT-$C_6H_3Cl_2$, which was suspended by 1% w/v sodium deoxycholate (DOC) while in all other cases the functionalized nanotubes were stabilized by 1 wt % SDS. Briefly, the concentration of (6,5)-SWCNTs was adjusted to give an optical density (OD) of 0.1 at the E_{11} absorption. A 4-nitrobenzenediazonium tetrafluoroborate ($4\text{-}C_6H_4NO_2N_2^+\cdot BF_4^-$) solution was then added to this nanotube solution for starting molar ratios of reactants, [Dz, diazonium]/[C, nanotube carbon], at 1:4,000, 1:2,500, 1:1,500, 1:1,000, 1:750, 1:500, and 1:250. These reactant ratios were slightly adjusted for the other diazonium salts to accommodate the difference in reactivity. The reaction occurs at room temperature with a pH of 5.5 and was monitored by following the defect photoluminescence with a NanoLog spectrofluorometer (Horiba Jobin Yvon) and ultraviolet/visible/near-infrared (UV−vis−NIR) absorption with a Lambda 1050 UV−vis−NIR spectrophotometer (PerkinElmer). The corresponding Raman D/G ratio was calculated from Raman spectra collected under both 532 and 633 nm excitation (LabRAM ARAMIS Raman microscope, Horiba Jobin Yvon).

Introduction of Oxygen Defects in SWCNTs. Oxygen dopants were introduced by following a doping protocol described previously.[6] ATP separated (6,5)-SWCNTs in 1 wt % SDBS (OD of 0.04 at E_{11}) were diluted with nanopure H_2O to a concentration of 0.2 wt % SDBS. Ozonated nanopure H_2O was then added with a volume ratio of 1:1. The reaction mixture was illuminated for 4 h by a quartz−tungsten halogen lamp and subsequently quenched by pressure filtration through a 100 kDa cellulose membrane using 1.04 wt % sodium deoxycholate (DOC) solution as eluate.

Exciton Evolution Probed by Temperature-Dependent Photoluminescence Spectroscopy. To probe the energy levels of fluorescent aryl defects, both the defect (E_{11}^-) and original (E_{11}) photoluminescence were collected as a function of solution temperature. The temperature of the

DOI: 10.1021/acs.jpcc.6b02538
J. Phys. Chem. C 2016, 120, 11268−11276

nanotube solution was controlled using a circulating water bath stage (FL-1027, Horiba Jobin Yvon). The temperature was measured with an immersion surface temperature sensor and LabQuest 2 (Vernier). At each 5 °C increment from 15 to 85 °C, a photoluminescence spectrum was collected. The E_{11} and E_{11}^- were fitted with Voigt profiles using Peakfit v4.12 (SeaSolve), and the integrated intensity ratios were plotted against temperature.

Quantum Chemical Modeling. The computations were performed using Gaussian 09 software suite.[19] A 10 nm long (6,5)-SWCNT segment, with open ends terminated by hydrogen atoms, was used. The system contained about 1000 carbon atoms. Density functional theory (DFT) calculations were done using Coulomb-attenuated B3LYP (CAM-B3LYP) functional[20] and STO-3G basis set. The optical transitions were computed using time-dependent DFT (TD-DFT). If not mentioned otherwise, the calculations were done in a vacuum. Some test cases have utilized solvent effects in the framework of conductor-like polarizable continuum medium model[21] using experimentally relevant water solvent. The functional group was added in the middle of the nanotube. In the case of oxygen doping, only the lowest energy structure (named ether-d in ref 4) was studied. In the case of aryl defects, we show the results for a special defect configuration consisting of a 4-bromoaryl ring and hydrogen atom added on the nearest-neighbor carbon along the tube axis. A detailed study of different atomic configurations of the defects is given in the Supporting Information.

RESULTS AND DISCUSSION

Controlled attachment of an aryl group to the nanotube surface creates a fluorescent sp^3 defect center within the sp^2 carbon lattice.[1] Figure 2a shows absorption and photoluminescence spectra of (6,5)-SWCNT-$C_6H_4NO_2$, produced from covalent functionalization of (6,5)-SWCNTs with small amounts of 4-nitrobenzenediazonium tetrafluoroborate. As the aryl defects are introduced, the original exciton PL (E_{11}, 981 nm) decreases and the defect PL (E_{11}^-) develops at a red-shifted position (1141 nm), whereas the E_{11} and E_{22} (second excitonic transition) absorption peaks only slightly weaken. An exciton that is trapped at this defect site can radiatively decay to produce a red-shifted emission (E_{11}^-) or escape the trap thermally (Figure 2b and Figure S1). Such exciton trapping and detrapping dynamics can be monitored by PL spectroscopy.

To determine the defect detrapping energy, we measured the PL spectra at 5 °C increments (over a temperature range from 15 to 85 °C) and constructed van 't Hoff plots based on the intensity ratio of the E_{11} and E_{11}^- PL as a function of temperature (Figure 2c,d). We note that the PL intensities discussed here are integrated PL intensities. The van 't Hoff analysis is routinely applicable to an effective two-level system at thermal equilibrium where at finite temperature the ratio of populations of two states is given by a Boltzmann exponent, $e^{-\Delta E/kT}$, where ΔE is the energy between the two states. For the case of SWCNTs that involve trapped (E_{11}^-) and free (E_{11}) excitons the situation is more complicated since the "upper state", i.e., the free exciton, is not a single state, or a discrete number of states, but a continuum of freely moving excitons with a thermal distribution of kinetic energies. The partition function for such a system is given by[22]

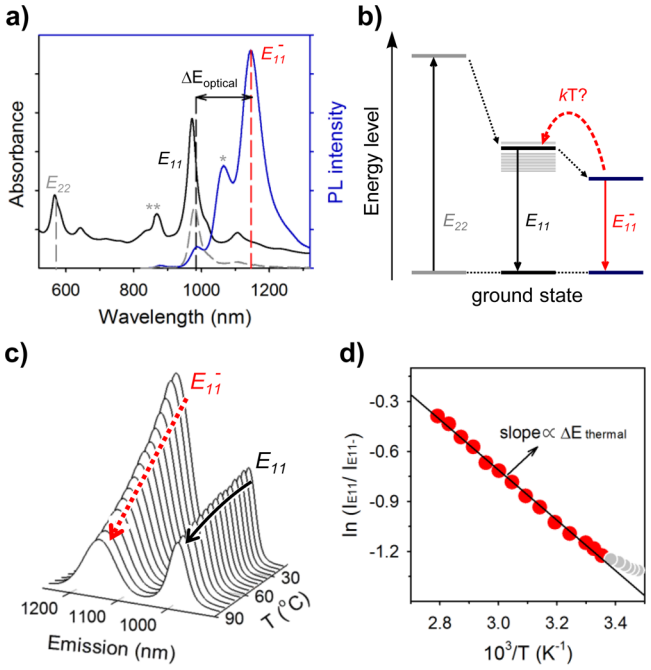

Figure 2. Thermodynamic probing of fluorescent aryl defects in semiconducting carbon nanotubes. (a) UV–vis–NIR absorption and vis–NIR photoluminescence spectra of (6,5)-SWCNT-$C_6H_4NO_2$ at room temperature. The dashed line is the PL spectrum of the unfunctionalized starting (6,5)-SWCNTs. The asterisked peaks are due to E_{11}^- PL and E_{11} absorption of (6,4)-SWCNTs. (b) Energy diagram of a SWCNT with a fluorescent defect: An exciton trapped at the defect level (E_{11}^-) can thermally escape the defect well and recombine *via* the bright singlet exciton channel (E_{11}). (c) Peak fitted PL spectra of (6,5)-SWCNT-$C_6H_4NO_2$ (synthesized at [Dz]:[C] = 1:500) at increasing temperatures with 5 °C increments. (d) The van 't Hoff plot as derived from the PL spectra in (c). Open circles are excluded from the calculations as they are dominated by surfactant reorganization effects.

$$Z = Z_t + Z_f = Ln_d + \frac{L}{\pi\hbar} e^{-\Delta E/kT} \left[\int_0^\infty dp\, e^{-p^2/2MkT} \right]^N \quad (1)$$

where the first right-hand side term is the number of defect sites (n_d is the concentration of defect sites and L is the SWCNT length). The dimensionality of the system is denoted by N (1 in the case of SWCNT). The second right-hand-side term represents the summation over the thermally excited free exciton states, where M is the exciton total mass, k is the Boltzmann constant, and T is temperature. The integral here can be evaluated exactly, leading to the ratio of trapped and free exciton populations as

$$\frac{p_f}{p_t} = \frac{Z_f}{Z_t} \propto T^{N/2} e^{-\Delta E/kT} \quad (2)$$

with the result being similar to the classical result for a thermally excited population of electrons in an extrinsic n-type semiconductor.[22] The ratio of populations in eq 2 is not exactly of the van 't Hoff type. However, the population of excitons is not what is directly accessed experimentally. Instead, what is analyzed is the ratio of photoluminescence intensities, which is essentially different from the ratio of populations if the oscillator strengths are temperature-dependent. The oscillator strength of the zero-dimensional trapped exciton is constant. However, thermally excited free excitons are decoupled from

DOI: 10.1021/acs.jpcc.6b02538
J. Phys. Chem. C 2016, 120, 11268–11276

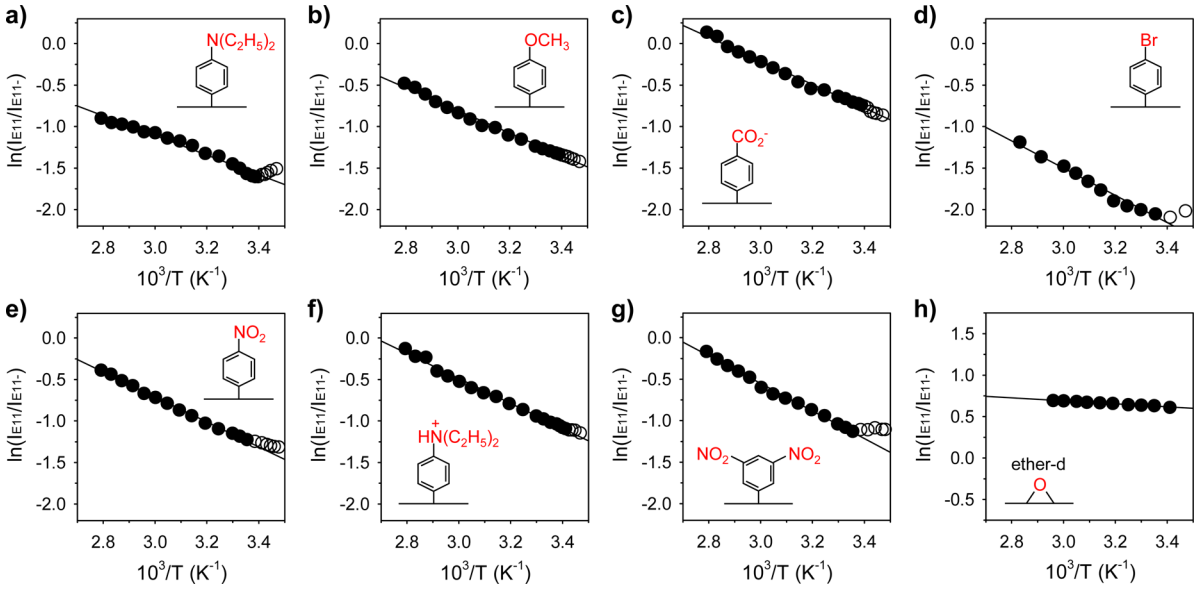

Figure 3. van 't Hoff plots for fluorescent quantum defect-labeled (6,5)-SWCNTs. The chemical nature of the defect is given in each plot. The defect density is maintained at a similar level for the aryl functional groups (a–g). The defect density for the O-doped sample (h) is at a lower level.

photons, so the average oscillator strength of free excitons in a 1D system (e.g., SWCNT) is proportional to $1/\sqrt{T}$.[23,24] The result is that the square roots of temperature, originating from the ratio of populations, and from the oscillator strength considerations, cancel each other, resulting in the ratio of PL intensities being the Boltzmann factor:

$$\frac{I_{E_{11}}}{I_{E_{11}^-}} \propto e^{-\Delta E/kT} \tag{3}$$

Therefore, the energy between the trapped and free excitonic states can be effectively derived by the van 't Hoff method. This energy difference is denoted as $\Delta E_{thermal}$ to differentiate it from the optical gap $\Delta E_{optical}$, which is determined from the emission energies. We note that this analysis neglects the possibility of dark exciton and trap states, which will introduce additional temperature dependences to observed PL intensities at low temperatures.[5,25,26] In the temperature range of our experiments, however, such an approximation is suitable. We further note that this van 't Hoff analysis can be skewed toward smaller $\Delta E_{thermal}$ if there exists an inhomogeneous distribution of trap depths. This effect is minimized here by integrating over the entire line width of the emission to better account for the contribution from the entire population of both native excitons and defect-trapped excitons. Quantification of this effect may be possible by applying similar techniques as developed by Graham *et al.* and Schilling *et al.* to determine the inhomogeneous broadening of the native exciton (E_{11}) band due to a distribution of energy barriers.[27,28]

Experimentally, we found that the PL of aryl-tailored nanotubes systematically responds to changes in the solution temperature. Above 25 °C, the PL intensity of both E_{11} and E_{11}^- gradually decrease with temperature (Figure 2c), but the relative decrease is more rapid for E_{11}^-. The behavior of E_{11} is due to the $1/\sqrt{T}$ intensity dependence, as discussed above, while the intensity loss in E_{11}^- arises from thermally induced exciton detrapping from the dopant site. As shown in Figure 2d, the integrated intensities of E_{11} and E_{11}^- PL are correlated with temperature by the following van 't Hoff relation, derived from eq 3:

$$\ln \frac{I_{E_{11}}}{I_{E_{11}^-}} = -\frac{\Delta E_{thermal}}{kT} + A' \tag{4}$$

where $I_{E_{11}}$ and $I_{E_{11}^-}$ are the integrated PL intensities of E_{11} and E_{11}^-, and A' is a correction factor. The slope of the van 't Hoff plot thus provides $\Delta E_{thermal}$ equal to 131 meV for (6,5)-SWCNT-$C_6H_4NO_2$.

The ability to synthetically tune the aryl dopants to alter optical properties provides a route to probe the generality and structural dependences of the $\Delta E_{thermal}$ behavior. We constructed van 't Hoff plots for a series of seven fluorescent aryl defects with different substituational moieties (Figure 3). In all cases, a good linear fit to eq 4 is found, allowing $\Delta E_{thermal}$ to be extracted for each dopant (see Table 1). We found that $\Delta E_{thermal}$ is linearly correlated with the electron-withdrawing and resonance capabilities of the moieties, as measured by the Hammett constant (σ_p).[29] As σ_p increases from −0.83 for 4-*N*,*N*-diethylamine to 1.42 for 3,5-dinitro, $\Delta E_{thermal}$ increases by 41 meV (Figure 4, red data, and also Table 1). This trend in $\Delta E_{thermal}$ closely traces what was observed with $\Delta E_{optical}$ (Figure 4, black data). As σ_p increases, the magnitude of $\Delta E_{optical}$ also increases (see also Table 1) and directly parallels the change observed in $\Delta E_{thermal}$. In our previous experiments it was concluded that a larger σ_p can effectively lower the E_{11}^- state, creating a deeper trap for excitons.[1] The linear correlation between $\Delta E_{thermal}$ and $\Delta E_{optical}$ thus consistently suggests that greater energy will be required for an exciton to thermally escape a deeper trap, as expected. Of significant interest, however, is the observation of a large energy offset of ~45 meV between $\Delta E_{thermal}$ and $\Delta E_{optical}$ that remains nearly constant for each type of aryl defect. Notably, in all cases the magnitude of the observed $\Delta E_{thermal}$ values are significantly lower (on the order of 70%) than the corresponding $\Delta E_{optical}$ values (Figure 4 and Table 1). This energy mismatch across the aryl defect series is also larger than that reported by the Weisman group for oxygen-doped nanotubes.[2] We note that in Figures 2d and 3, for temperatures below 25 °C, the intensity ratio of E_{11} to E_{11}^- begins to rise again as temperature is lowered further. This behavior is likely due to surfactant reorganization at low

DOI: 10.1021/acs.jpcc.6b02538
J. Phys. Chem. C 2016, 120, 11268–11276

Table 1. Tabulation of Trap Site Optical Emission Energies (E_{11}^-), $\Delta E_{optical}$, Thermally Determined Trapping Energies ($\Delta E_{thermal}$), and Experimentally Determined Reorganization Energies (λ) for Various Fluorescent Defects (X)

X[b]	E_{11} (nm)	E_{11}^- (nm)	$\Delta E_{optical}$ (meV)	$\Delta E_{thermal}$ (meV)	λ (meV)
O-doped (low)[a]	994	1125	146	24	122
$-NEt_2$	989	1127	154	102	52
3,5-Cl_2 (low)[a]	992	1133	155	35	120
3,5-Cl_2 (high)[a]	992	1133	155	134	21
$-OCH_3$	988	1130	158	117	41
$-CO_2^-$	992	1143	165	123	42
$-Br$	988	1143	170	149	21
$-NO_2$ (low)[a]	982	1139	174	76	98
$-NO_2$ (high)[a]	981	1141	177	131	46
$-HNEt_2^+$	989	1146	172	130	42
3,5-$(NO_2)_2$	988	1163	189	143	46

[a]Values for $\Delta E_{thermal}$ and λ for these fluorescent defects are given for high and/or low defect density cases. The low density limit is most directly comparable to the DFT results of Table 2. All other values were obtained at relatively high defect densities, where $I_{E_{11}^-}/I_{E_{11}} > 2$ at 25 °C. [b]X represents the terminating moieties of an aryl defect except for an oxygen dopant (ether-d).

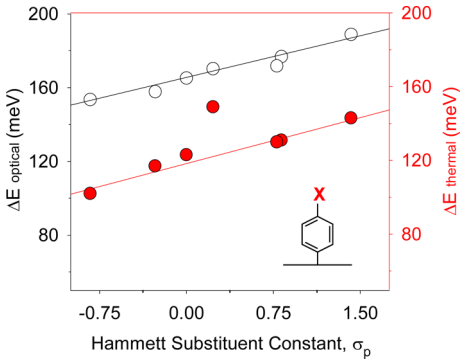

Figure 4. Correlations of optical gaps ($\Delta E_{optical}$, black open circles) and thermal detrapping energies ($\Delta E_{thermal}$, red closed circles) as functions of the chemical nature (as measured by Hammett substituent constant, σ_p) of fluorescent aryl defects. The defect density of each (6,5)-SWCNT sample was adjusted to produce $I_{E_{11}^-}/I_{E_{11}} > 2$.

temperatures[30−33] or may arise from a dark defect state existing below the emitting state (as suggested in ref 5) and is the subject of ongoing study in our lab.

The energy mismatch between $\Delta E_{thermal}$ and $\Delta E_{optical}$ is now seen as a general phenomenon over a wide range of defect-tailored SWCNTs. As a route to a more in-depth understanding on the origins of this energy mismatch, we employ density functional theory to model the energies of the relevant states and transformations between them within a molecular picture of the defect site. Toward this goal, it is first instructive to view the energy diagram of Figure 2a in terms of overlapping molecular-like potential surfaces for free and trapped excitons (see Figure 5). Such a molecular view has been demonstrated as useful for understanding certain aspects of free exciton behavior in carbon nanotubes[34] and is particularly appropriate for an exciton localized at a trap site. Within this view, the energy mismatch may be interpreted to arise from major contributions from reorganization energy at the defect site.

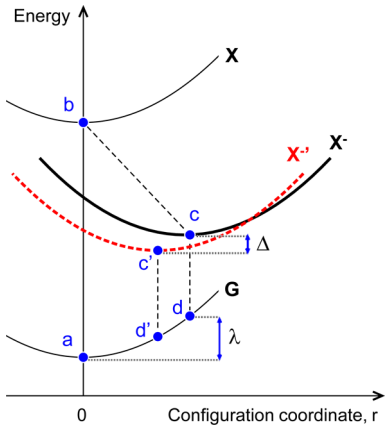

Figure 5. Potential energy surfaces for ground (G), trapped exciton (X^-), and free exciton (X). "Configuration coordinate" r (horizontal axis) denotes the deformation (reorganization) of the SWCNT geometry. Here the reorganization energy is dominated by displacement of nuclear coordinates since changes in vibration frequency, or curvature of potentials, are negligible in rigid systems such as SWCNTs. Note that the energy separations between the states are not to scale and the red curve is for a trapped exciton delocalized over two defect sites.

Consider the electronic terms of our system. These may include the potential energy surfaces for the ground state (G), defect-trapped (X^-) exciton, and free exciton (X), as schematically presented in Figure 5. The "configuration coordinate" (r) has been arbitrarily chosen as zero at the optimal ground state geometry, so that the energy minimum of the ground state parabola is located at $r = 0$. Thus, coordinate r represents the distortion of the SWCNT geometry relative to the ground state geometry. Following initial optical excitation to X, diffusional transport to a defect site results in exciton trapping and relaxation to state X^-.[4−6] We focus on energies associated with thermal activation out of X^- to X or relaxation from X^- to G *via* emission of a photon.

Because of exciton−phonon coupling, the minima of the excited state parabolas are in general located at finite r. Trap-state PL originates from the optimal geometry of the X^- state (point c in Figure 5). Because of the Franck−Condon principle, the optical transitions are "vertical." The defect state emission process therefore occurs between point "c" of the X^- curve and point "d" of the ground state surface, with energy $E_{cd} = E_c - E_d$. Point "d" represents an excited state geometric configuration of the ground state surface. Its energy difference with the ground state equilibrium configuration at point "a" (E_{da}) represents the reorganization energy λ for the transition between X^- and G electronic terms. Our defined $\Delta E_{optical}$ ($= E_{11} - E_{11}^-$) is therefore equivalent to $E_{ba} - E_{cd}$.

Thermal activation out of the trap state, on the other hand, is a slow process relative to optical excitation, and the Franck−Condon principle is thus invalid for thermal detrapping. The required thermal activation energy is therefore equivalent to the energy difference between the minima of the X and X^- curves: $E_{bc} = \Delta E_{thermal}$. Referring to Figure 5, the difference between the optical and thermal activation energies is given as

$$\Delta E_{optical} - \Delta E_{thermal} = (E_{ba} - E_{cd}) - E_{bc} = E_{da} = \lambda > 0 \quad (5)$$

We note that in arriving at eq 5, we have neglected for simplicity any independent reorganization energy associated

DOI: 10.1021/acs.jpcc.6b02538
J. Phys. Chem. C 2016, 120, 11268−11276

with optical excitation of the initial E_{11} excited state at point "b" of the X curve. This is a reasonable approximation, as the relatively delocalized nature of the E_{11} exciton (in contrast to that of the trap state) naturally leads to a reduced reorganization energy. Such a simplification is supported by experimental observations of small Stokes shifts (~8 meV) in E_{11} emission[35] and by Raman studies showing weak exciton−phonon coupling.[36]

Inspection of Figure 5 thus suggests that the origin of the mismatch in $\Delta E_{optical}$ vs $\Delta E_{thermal}$ is due to a reorganization energy component associated with the optical transition. Such an energy cost is expected from the associated large coordinate changes that should arise from significant localization of the exciton wave function imposed by trapping.[4,6] We note that while we have discussed changes in the reaction coordinate r (Figure 5) as arising from a distortion of the SWCNT geometry, other contributions can exist, including solvent polarization and surfactant reorganization as examples. Any such contribution can only increase the total observable reorganization energy, so the final expression for the difference between the optical gap and the detrapping energy would be

$$\Delta E_{optical} - \Delta E_{thermal} = \sum_i \lambda_i > 0 \quad (6)$$

where each contribution λ_i is positive. From the measured $\Delta E_{thermal}$ and $\Delta E_{optical}$, we can further derive that the reorganization energy can be on the order of 50 meV (Figure 4 and Table 1) and, in the limit of low defect density, can be as large as 100 meV. While $\Delta E_{optical}$ and $\Delta E_{thermal}$ have similar origins in the trap state, they are nevertheless physically distinct, as they describe vertical and nonvertical transitions, respectively. In particular, eqs 5 and 6 imply that $\Delta E_{optical}$ is always larger than $\Delta E_{thermal}$, which is consistent with our experimental observations and those of Ghosh *et al.*[2] Furthermore, it is important to recognize that our proposed model based on Figure 5 indicates that the experimentally determined thermal barrier most closely equates to the actual depth of the trapping potential. As described below, our DFT results further support this interpretation.

Our previous computational studies of oxygen-doped or defect-tailored carbon nanotubes have provided a detailed view on the structure and properties of SWCNT excited states and electronic levels at defect sites.[1,3,4,6,37,38] Here we focus on the vibrational relaxation of ground and excited electronic states in representative examples. The reorganization energy (λ) is computed as the difference of total energies of the system in the ground state, at the ground state optimal geometry (r = 0 in Figure 5) and in the ground state, but at the configuration coordinate (r) corresponding to the optimal geometry of the excited state X^- (point d in Figure 5), which directly corresponds to the definition given by eq 5 (see also Figure S5). Ground and excited state optimal geometries were obtained using DFT and time-dependent DFT (TD-DFT) formalisms, respectively (Figures S6 and S7). The relevant computational details are provided in the Experimental Section. In addition to the pristine 10 nm long (6,5) tube, we have considered oxygen-doped (ether-d) and 4-bromoaryl ($-C_6H_4Br$) defect-tailored species. Additionally, detailed discussion on various possible geometries and computational methodologies is provided in the Supporting Information. In the pristine tube we consider the lowest electronic states. Here the calculated λ of the E_{11} exciton is 13 meV. This supports our earlier approximation where this quantity was neglected. When defects are introduced, we observe lower energy electronic states in our calculations. Specifically, the lowest state (E_{11}^-) in the aryl defect tailored tube has substantial oscillator strength and thus is emissive. In stark contrast to the E_{11} exciton of a pristine tube, λ for E_{11}^- is substantially larger, being 101 meV (see Table 2).

Table 2. Calculated Reorganization Energies for Pristine and Doped (6,5)-SWCNTs

dopant system	λ (meV)
pristine	13
ether-d (state 1, dark)	18
ether-d (state 2, bright)	70
2 × (C_6H_4Br + H) (1 nm spacing)	28
2 × (C_6H_4Br + H) (2 nm spacing)	78
2 × (C_6H_4Br + H) (3 nm spacing)	92
isolated $-C_6H_4Br$ + H	101
isolated $-C_6H_4Br$ + H with solvent	125

Reference 5 suggests the occurrence of bright and optically forbidden (dark) defect states for oxygen-doped tubes. Our DFT results also indicate this. Interestingly, for oxygen-doped nanotubes the dark defect state is energetically below the emissive state while for aryl defects, the bright defect state is the lowest. At the optimal geometry of the dark state, we find the lowest electronic transition in oxygen-doped tubes in the ether-d geometry is this dark state, whereas the optically allowed E_{11}^- transition is state number 2. The calculated splitting between these bright and dark states at this geometry is 13 meV. These results are in agreement with ref 5, which suggested the existence of a dark state at 16 meV below the E_{11}^- transition for oxygen-doped tubes. We calculate a small λ of 18 meV in the ether-d geometry for the dark state. In contrast, at the optimal geometry for the bright state, the ordering of the states is reversed, with the bright state found to cross the dark state and become the lowest energy dopant state. The bright state optimized geometry is found to occur at a larger configuration coordinate (r, Figure 5). Consequently, the reorganization energy of the bright E_{11}^- transition (70 meV) is larger than that of the lowest energy dopant state for oxygen-doped SWCNTs.

To rationalize the observed trends in λ and to link them to the underlying wave function properties, we further analyze calculated transition density matrices corresponding to the excitonic wave functions of the excited states. These quantities for native E_{11}, ether-d E_{11}^-, and 4-bromoaryl defect E_{11}^- excitons are depicted in Figure 6a−c, respectively. In these plots, the horizontal and vertical axes correspond to electron and hole coordinates, respectively. The diagonal size of the matrix corresponds to the delocalization of exciton wave function along the SWCNT axis, and the width of the matrix reflects electron−hole separation, which is about 1−2 nm in all cases. We observe that the native E_{11} exciton is delocalized over about 6 nm (Figure 6a). For the dark E_{11}^- exciton in the oxygen-doped tube (state 1) we find a localization to about 3 nm in size (Figure 6b). Moreover, both the bright E_{11}^- excitons in the oxygen-doped tube (state 2) and for the aryl defect tailored tube are localized even more, on about a 1 nm length scale (see Figure 6c). Such spatial localization of the wave function effectively increases the amount of exciton−phonon coupling and thus increases reorganization energy across these cases.

Finally, we investigated computationally the effect of defect density in aryl defect tailored SWCNTs on the value of λ. We

DOI: 10.1021/acs.jpcc.6b02538
J. Phys. Chem. C 2016, 120, 11268−11276

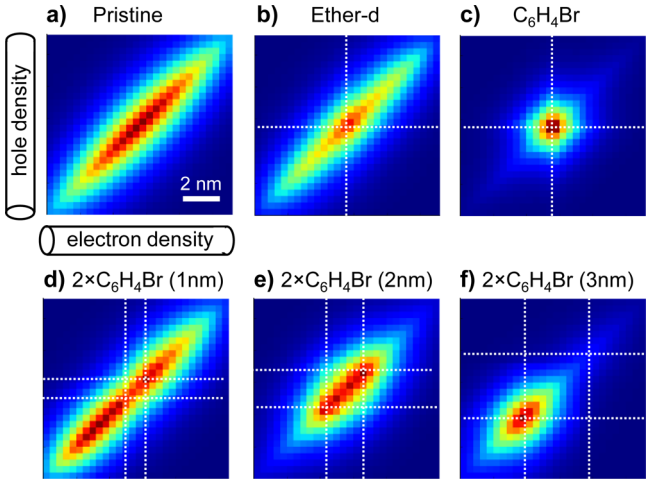

Figure 6. Exciton plots of optically active states in a pristine (6,5)-SWCNT (a) and the lowest electronic transitions for oxygen-doped (b) and 4-bromoaryl defect (denoted as $-C_6H_4Br$) tailored (c-f) 10 nm long (6,5)-SWCNTs. Horizontal (vertical) axis corresponds to the distribution of electron (hole) density along nanotube axis. White dashed lines mark the positions of dopants. The size of one pixel is 0.4 nm.

have used two C_6H_4Br + H defects on a single (6,5)-SWCNT separated by 1, 2, and 3 nm distance. The computational results are summarized in Table 2. Our analysis shows that if the two defect sites are situated closely to each other, at distances comparable to the exciton size at the defect site, their electronic states overlap and strongly interact. Subsequently, the lowest optical transition with E_{11}^- character becomes delocalized between the two sp^3 defects as shown in Figure 6d, suggesting a reduced exciton−phonon coupling. As a result, the reorganization energy is strongly reduced from 101 to 28 meV. When the distance between defects increases, λ gradually increases and approaches the value found for isolated sp^3 defects (~100 meV). For example, λ is equal to 78 meV for defects separated by 2 nm distance. Here, the exciton wave function is contained to about 2 nm length (Figure 6e). For larger separation distances, the defect sites become uncorrelated and the vibrational dynamics is contained to a single site. For example, Figure 6f shows that the exciton is localized on one of the sp^3 defects, and its wave function resembles the isolated defect site case (Figure 6c). The reorganization energy for a system with two sp^3 defects, separated by 3 nm, is 92 meV, approaching that of an isolated defect of 101 meV. The computed trend for λ suggests that observed reorganization energy (the difference between $\Delta E_{optical}$ and $\Delta E_{thermal}$) should depend on the defect density. This predicted trend in fact agrees with our experimental results.

We confirmed this theoretical prediction experimentally by measuring $\Delta E_{thermal}$ in (6,5)-SWCNT-$C_6H_4NO_2$ as a function of the defect density (Figure S2). The defect density is chemically controlled simply by changing the [Dz]:[C] reactant ratio and quantified by Raman spectroscopy (Figure S3). The Raman D/G ratio is directly correlated with the defect density because the D phonon mode (at ~1300 cm^{-1}) is due to symmetry breaking by the covalently attached aryl groups while the G band (~1590 cm^{-1}) is an in-plane stretching mode of the sp^2-bonded carbon lattice.[39] As SWCNTs react with increasing amounts of 4-nitrobenzenediazonium salts, the D/G ratio proportionally increases, consistent with previously reported trends in the reaction of (6,5)-SWCNTs with 4-bromobenzenediazonium salts.[1] From the constructed van 't Hoff plots, we found that the slopes ($\Delta E_{thermal}$) are linearly correlated with the defect density (Figure 7). The $\Delta E_{optical}$ is only weakly

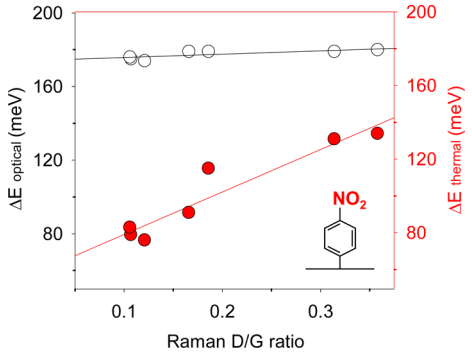

Figure 7. $\Delta E_{optical}$ (open black circles) and $\Delta E_{thermal}$ (closed red circles) as a function of defect density (as measured by the Raman D/G intensity ratio, defect density increases with D/G).

dependent on the defect density, with a change of only 5 meV across the range of densities explored. In contrast, $\Delta E_{thermal}$ is strongly affected by the density of defects, varying from 76 meV at the lowest density (synthesized at [Dz]:[C] = 1:2500) to 134 meV at the highest (synthesized at [Dz]:[C] = 1:250). At the lowest defect density that can be experimentally measured in (6,5)-SWCNT-$C_6H_4NO_2$, the mismatch (λ) between $\Delta E_{thermal}$ and $\Delta E_{optical}$ is as large as 98 meV, in close agreement with the DFT results for the isolated defect case (see Table 2). Similar results were obtained with a defect density series based on the 3,5-dichloroaryl defects as well, for which a λ value of 120 meV was determined in the low defect density limit, again in agreement with the DFT results (Figures S2 and S4). We also note that the oxygen dopant result of Figure 3h was obtained in this low defect density limit, thus providing an explanation for the difference in our result for $\Delta E_{thermal}$ (24 meV) compared to that initially reported in the work of Ghosh *et al.* (61 meV).[2]

At high defect densities, there is a finite probability that a single trapped exciton can be delocalized over two (or more) defect sites. This probability is small if the position of defects is completely random along the SWCNT. However, the probability can increase if the functional groups do effectively interact with each other; for instance, during a propagative reaction a second functional group has a high probability to attach to a SWCNT near the first defect.[40] Evidence of defect coupling is suggested by the gradual, but nevertheless persistent, red-shift (by 5 meV in Figure 7) and peak broadening (from 44.7 to 73.2 ± 7.9 meV at 30 °C) of the E_{11}^- PL at increasing defect densities.

As indicated by our DFT results, there are two consequences of a trapped exciton being delocalized over two defect sites. First, at fixed ground state geometry its electronic energy decreases due to the delocalization of the trapped exciton. As a result, the corresponding X^- parabola in Figure 5 would shift downward in energy by an amount Δ. Second, due to the decrease of the electron−phonon interaction upon the delocalization, the minimum of the resulting parabola shifts toward $r = 0$. The resulting potential energy surface is shown by a red dashed parabola in Figure 5. The corresponding reorganization energy $\lambda' = E_{d'a}$ is smaller than the original λ.

DOI: 10.1021/acs.jpcc.6b02538
J. Phys. Chem. C 2016, 120, 11268−11276

These two results have consequences for the observed behavior of both E_{11}^{-} and $\Delta E_{thermal}$.

For a trapped exciton that is delocalized over two (or more) defect sites, E_{11}^{-} and $\Delta E_{thermal}$ energies become

$$E_{11}^{-'} = E_{c'd'} = E_{11}^{-} - \Delta + (\lambda - \lambda') \quad (7)$$

$$\Delta E'_{thermal} = E_{bc'} = \Delta E_{thermal} + \Delta \quad (8)$$

and E_{11} remains the same if the concentration of defects is not large enough to significantly alter the ground and excited states of the entire SWCNT (this is observed experimentally). Equation 7 shows that the trap state emission energy, while red-shifted by the coupling between interacting sites, may be offset in the opposite direction by the reorganizational change accompanying the expected exciton delocalization at higher dopant densities. Our experimental observation of only minor changes in E_{11}^{-} as defect density is increased indicates these two effects nearly balance each other. As seen in eq 8, on the other hand, $\Delta E_{thermal}$ is affected only by changes in Δ. Thus, the detrapping energy extracted from the van 't Hoff plots is expected to steadily increase with the defect density.

CONCLUSION

We observed a substantial mismatch between optical energy gap and thermally determined detrapping energy in a series of fluorescent aryl defects that are chemically incorporated in semiconducting carbon nanotubes. Both the optical gap and the detrapping energy reveal a linear correlation with the electron withdrawing/donating capability of the aryl substituents. However, depending on the chemical nature and density of the defect, the detrapping energy is 14−77% smaller than the optical gap. For the same type of defect on (6,5)-SWCNTs, the detrapping energy varies from 76 to 131 meV depending on the defect density, whereas the optical gap is nearly independent (<5 meV). For each aryl defect at a similar defect density, the mismatch is a nearly constant 48 ± 5 meV.

The observed energy mismatches can be understood in terms of vibrational reorganization due to significant deformation of the nanotube geometry upon exciton trapping at the defect site. The reorganization energy is experimentally determined to be as large as 100 meV for (6,5)-SWCNT-$C_6H_4NO_2$ and 120 meV for (6,5)-SWCNT-$C_6H_3(NO_2)_2$ and is strongly dependent on the defect density. These experimental findings are analyzed with our electronic structure simulations, which map the observed trends into dopant-dependent vibrational reorganization energy in the molecular picture. Our findings are consistent with spectroelectrochemical measurements from oxygen-doped SWCNTs that show smaller redox potential than the optical energy gap[9] and provide new insights into the origin of the large discrepancy between optical gap and detrapping energy in fluorescent nanotube defect systems. These insights establish a comprehensive picture of the energetics of fluorescent defects in SWCNTs, of direct relevance for the mechanistics of recently reported photon upconversion processes in defect-tailored SWCNTs,[13] and may help guide the design and synthesis of molecularly tunable fluorescent quantum defects[41] for applications in near-infrared bioimaging, sensing,[11] energy harvesting,[13] and single photon sources.[14,15]

ASSOCIATED CONTENT

Supporting Information

The Supporting Information is available free of charge on the ACS Publications website at DOI: 10.1021/acs.jpcc.6b02538.

van 't Hoff plots for various defect densities, correlated PL and Raman scattering, and details on density functional theory calculations (PDF)

AUTHOR INFORMATION

Corresponding Authors

*(Y.H.W.) Tel +1-301-405-3368; Fax +1-301-314-9121; e-mail yhw@umd.edu.

*(S.K.D.) Tel +1-505-667-2541; e-mail skdoorn@lanl.gov.

Notes

The authors declare no competing financial interest.

ACKNOWLEDGMENTS

This work was supported by the National Science Foundation (CHE-1507974, CAREER CHE-1055514). CNT sorting is supported by AFOSR through MURI grant FA9550-16-1-0150. S.K.D. and S.T. acknowledge partial support from the LANL LDRD program. This work was performed in part at the Center for Integrated Nanotechnologies, a U.S. Department of Energy, Office of Science user facility, as part of User Project U2015A0059. The authors also acknowledge the LANL Institutional Computing (IC) Program for providing computational resources.

REFERENCES

(1) Piao, Y.; Meany, B.; Powell, L. R.; Valley, N.; Kwon, H.; Schatz, G. C.; Wang, Y. Brightening of Carbon Nanotube Photoluminescence through the Incorporation of sp^3 Defects. *Nat. Chem.* **2013**, *5*, 840−845.

(2) Ghosh, S.; Bachilo, S. M.; Simonette, R. A.; Beckingham, K. M.; Weisman, R. B. Oxygen Doping Modifies Near-Infrared Band Gaps in Fluorescent Single-Walled Carbon Nanotubes. *Science* **2010**, *330*, 1656−1659.

(3) Zhang, Y.; Valley, N.; Brozena, A. H.; Piao, Y.; Song, X.; Schatz, G. C.; Wang, Y. Propagative Sidewall Alkylcarboxylation that Induces Red-Shifted Near-IR Photoluminescence in Single-Walled Carbon Nanotubes. *J. Phys. Chem. Lett.* **2013**, *4*, 826−830.

(4) Ma, X.; Adamska, L.; Yamaguchi, H.; Yalcin, S. E.; Tretiak, S.; Doorn, S. K.; Htoon, H. Electronic Structure and Chemical Nature of Oxygen Dopant States in Carbon Nanotubes. *ACS Nano* **2014**, *8*, 10782−10789.

(5) Miyauchi, Y.; Iwamura, M.; Mouri, S.; Kawazoe, T.; Ohtsu, M.; Matsuda, K. Brightening of Excitons in Carbon Nanotubes on Dimensionality Modification. *Nat. Photonics* **2013**, *7*, 715−719.

(6) Hartmann, N. F.; Yalcin, S. E.; Adamska, L.; Haroz, E. H.; Ma, X.; Tretiak, S.; Htoon, H.; Doorn, S. K. Photoluminescence Imaging of Solitary Dopant Sites in Covalently Doped Single-Wall Carbon Nanotubes. *Nanoscale* **2015**, *7*, 20521−20530.

(7) Iwamura, M.; Akizuki, N.; Miyauchi, Y.; Mouri, S.; Shaver, J.; Gao, Z.; Cognet, L.; Lounis, B.; Matsuda, K. Nonlinear Photoluminescence Spectroscopy of Carbon Nanotubes with Localized Exciton States. *ACS Nano* **2014**, *8*, 11254−11260.

(8) Ohfuchi, M. Ab Initio Study on Oxygen Doping of (5,4), (6,4), (6,5), and (8,6) Carbon Nanotubes. *J. Phys. Chem. C* **2015**, *119*, 13200−13206.

(9) Shiraishi, T.; Juhász, G.; Shiraki, T.; Akizuki, N.; Miyauchi, Y.; Matsuda, K.; Nakashima, N. Determination of Precise Redox Properties of Oxygen-Doped Single-Walled Carbon Nanotubes Based on in Situ Photoluminescence Electrochemistry. *J. Phys. Chem. C* **2015**, DOI: 10.1021/acs.jpcc.5b07841.

(10) Brozena, A. H.; Leeds, J. D.; Zhang, Y.; Fourkas, J. T.; Wang, Y. Controlled Defects in Semiconducting Carbon Nanotubes Promote Efficient Generation and Luminescence of Trions. *ACS Nano* **2014**, *8*, 4239−4247.
(11) Kwon, H.; Kim, M.; Meany, B.; Piao, Y.; Powell, L. R.; Wang, Y. Optical Probing of Local pH and Temperature in Complex Fluids with Covalently Functionalized, Semiconducting Carbon Nanotubes. *J. Phys. Chem. C* **2015**, *119*, 3733−3739.
(12) Wilson, H.; Ripp, S.; Prisbrey, L.; Brown, M. A.; Sharf, T.; Myles, D. J.; Blank, K. G.; Minot, E. D. Electrical Monitoring of sp^3 Defect Formation in Individual Carbon Nanotubes. *J. Phys. Chem. C* **2016**, *120*, 1971−1976.
(13) Akizuki, N.; Aota, S.; Mouri, S.; Matsuda, K.; Miyauchi, Y. Efficient Near-Infrared Up-Conversion Photoluminescence in Carbon Nanotubes. *Nat. Commun.* **2015**, *6*, 8920.
(14) Ma, X.; Hartmann, N. F.; Baldwin, J. K. S.; Doorn, S. K.; Htoon, H. Room-Temperature Single-Photon Generation from Solitary Dopants of Carbon Nanotubes. *Nat. Nanotechnol.* **2015**, *10*, 671−675.
(15) Ma, X.; Baldwin, J. K. S.; Hartmann, N. F.; Doorn, S. K.; Htoon, H. Solid-State Approach for Fabrication of Photostable, Oxygen-Doped Carbon Nanotubes. *Adv. Funct. Mater.* **2015**, *25*, 6157−6164.
(16) Liu, H.; Nishide, D.; Tanaka, T.; Kataura, H. Large-Scale Single-Chirality Separation of Single-Wall Carbon Nanotubes by Simple Gel Chromatography. *Nat. Commun.* **2011**, *2*, 309.
(17) Subbaiyan, N. K.; Cambré, S.; Parra-Vasquez, A. N. G.; Hároz, E. H.; Doorn, S. K.; Duque, J. G. Role of Surfactants and Salt in Aqueous Two-Phase Separation of Carbon Nanotubes toward Simple Chirality Isolation. *ACS Nano* **2014**, *8*, 1619−1628.
(18) Subbaiyan, N. K.; Parra-Vasquez, A. N. G.; Cambré, S.; Cordoba, M. A. S.; Yalcin, S. E.; Hamilton, C. E.; Mack, N. H.; Blackburn, J. L.; Doorn, S. K.; Duque, J. G. Bench-Top Aqueous Two-Phase Extraction of Isolated Individual Single-Walled Carbon Nanotubes. *Nano Res.* **2015**, *8*, 1755−1769.
(19) Frisch, M. J.; Trucks, G. W.; Schlegel, H. B.; Scuseria, G. E.; Robb, M. A.; Cheeseman, J. R.; Scalmani, G.; Barone, V.; Mennucci, B.; Petersson, G. A.; et al. *Gaussian 09*; Gaussian, Inc.: Wallingford, CT, 2009.
(20) Yanai, T.; Tew, D. P.; Handy, N. C. A New Hybrid Exchange−Correlation Functional Using the Coulomb-Attenuating Method (CAM-B3LYP). *Chem. Phys. Lett.* **2004**, *393*, 51−57.
(21) Cossi, M.; Rega, N.; Scalmani, G.; Barone, V. Energies, Structures, and Electronic Properties of Molecules in Solution with the C-PCM Solvation Model. *J. Comput. Chem.* **2003**, *24*, 669−681.
(22) Blakemore, J. S. *Semiconductor Statistics*; Pergamon Press: Oxford, UK, 1962.
(23) Perebeinos, V.; Tersoff, J.; Avouris, P. Radiative Lifetime of Excitons in Carbon Nanotubes. *Nano Lett.* **2005**, *5*, 2495−2499.
(24) Mouri, S.; Miyauchi, Y.; Iwamura, M.; Matsuda, K. Temperature Dependence of Photoluminescence Spectra in Hole-Doped Single-Walled Carbon Nanotubes: Implications of Trion Localization. *Phys. Rev. B: Condens. Matter Mater. Phys.* **2013**, *87*, 045408.
(25) Berciaud, S.; Cognet, L.; Lounis, B. Luminescence Decay and the Absorption Cross Section of Individual Single-Walled Carbon Nanotubes. *Phys. Rev. Lett.* **2008**, *101*, 077402.
(26) Matsunaga, R.; Miyauchi, Y.; Matsuda, K.; Kanemitsu, Y. Symmetry-Induced Nonequilibrium Distributions of Bright and Dark Exciton States in Single Carbon Nanotubes. *Phys. Rev. B: Condens. Matter Mater. Phys.* **2009**, *80*, 115436.
(27) Graham, M. W.; Ma, Y. Z.; Green, A. A.; Hersam, M. C.; Fleming, G. R. Pure Optical Dephasing Dynamics in Semiconducting Single-Walled Carbon Nanotubes. *J. Chem. Phys.* **2011**, *134*, 034504.
(28) Schilling, D.; Mann, C.; Kunkel, P.; Schöppler, F.; Hertel, T. Ultrafast Spectral Exciton Diffusion in Single-Wall Carbon Nanotubes Studied by Time-Resolved Hole Burning. *J. Phys. Chem. C* **2015**, *119*, 24116−24123.
(29) Hansch, C.; Leo, A.; Taft, R. W. A Survey of Hammett Substituent Constants and Resonance and Field Parameters. *Chem. Rev.* **1991**, *91*, 165−195.
(30) Hammouda, B. Temperature Effect on the Nanostructure of SDS Micelles in Water. *J. Res. Natl. Inst. Stand. Technol.* **2013**, *118*, 151−167.
(31) Niyogi, S.; Densmore, C. G.; Doorn, S. K. Electrolyte Tuning of Surfactant Interfacial Behavior for Enhanced Density-Based Separations of Single-Walled Carbon Nanotubes. *J. Am. Chem. Soc.* **2009**, *131*, 1144−1153.
(32) Siitonen, A. J.; Tsyboulski, D. A.; Bachilo, S. M.; Weisman, R. B. Surfactant-Dependent Exciton Mobility in Single-Walled Carbon Nanotubes Studied by Single-Molecule Reactions. *Nano Lett.* **2010**, *10*, 1595−1599.
(33) Li, L. J.; Nicholas, R. J.; Chen, C. Y.; Darton, R. C.; Baker, S. C. Comparative Study of Photoluminescence of Single-Walled Carbon Nanotubes Wrapped with Sodium Dodecyl Sulfate, Surfactin and Polyvinylpyrrolidone. *Nanotechnology* **2005**, *16*, S202−S205.
(34) Duque, J. G.; Chen, H.; Swan, A. K.; Shreve, A. P.; Kilina, S.; Tretiak, S.; Tu, X.; Zheng, M.; Doorn, S. K. Violation of the Condon Approximation in Semiconducting Carbon Nanotubes. *ACS Nano* **2011**, *5*, 5233−5241.
(35) Jones, M.; Engtrakul, C.; Metzger, W. K.; Ellingson, R. J.; Nozik, A. J.; Heben, M. J.; Rumbles, G. Analysis of Photoluminescence from Solubilized Single-Walled Carbon Nanotubes. *Phys. Rev. B: Condens. Matter Mater. Phys.* **2005**, *71*, 115426.
(36) Shreve, A. P.; Haroz, E. H.; Bachilo, S. M.; Weisman, R. B.; Tretiak, S.; Kilina, S.; Doorn, S. K. Determination of Exciton-Phonon Coupling Elements in Single-Walled Carbon Nanotubes by Raman Overtone Analysis. *Phys. Rev. Lett.* **2007**, *98*, 037405.
(37) Kilina, S.; Ramirez, J.; Tretiak, S. Brightening of the Lowest Exciton in Carbon Nanotubes *via* Chemical Functionalization. *Nano Lett.* **2012**, *12*, 2306−2312.
(38) Ramirez, J.; Mayo, M. L.; Kilina, S.; Tretiak, S. Electronic Structure and Optical Spectra of Semiconducting Carbon Nanotubes Functionalized by Diazonium Salts. *Chem. Phys.* **2013**, *413*, 89−101.
(39) Dresselhaus, M. S.; Dresselhaus, G.; Saito, R.; Jorio, A. Raman Spectroscopy of Carbon Nanotubes. *Phys. Rep.* **2005**, *409*, 47−99.
(40) Deng, S.; Zhang, Y.; Brozena, A. H.; Mayes, M. L.; Banerjee, P.; Chiou, W.-A.; Rubloff, G. W.; Schatz, G. C.; Wang, Y. Confined Propagation of Covalent Chemical Reactions on Single-Walled Carbon Nanotubes. *Nat. Commun.* **2011**, *2*, 382.
(41) Kwon, H.; Furmanchuk, A.; Kim, M.; Meany, B.; Guo, Y.; Schatz, G. C.; Wang, Y. Molecularly Tunable Fluorescent Quantum Defects. *J. Am. Chem. Soc.* **2016**, DOI: 10.1021/jacs.6b03618.

DOI: 10.1021/acs.jpcc.6b02538
J. Phys. Chem. C 2016, 120, 11268−11276